



Simulation of local metastable microstructural states in large tools: construction and validation of the model

Jannik Schuppener¹ · Aaron Berger¹ · Santiago Benito¹ · Sebastian Weber¹

Received: 30 May 2023 / Accepted: 19 August 2023 / Published online: 29 August 2023
© The Author(s) 2023

Abstract

This study presents the development and experimental verification of a simulation model for estimating the local microstructure of a tool geometry after heat treatment. The experiment involved subjecting a metallic block of dimensions $40 \times 50 \times 50$ mm, made of the ledeburitic cold work steel DIN EN 1.2379 (X153CrMoV12; AISI D2), to a heat treatment in a laboratory furnace at 1000 °C for 20 min. Thermocouples were strategically placed to record time-temperature profiles at different locations within the block. Following the heat treatment, the local microstructure was determined through quantitative image analysis, and the local hardness was measured as a function of the distance from the block's edge to its core. These measurements were then correlated with the corresponding time-temperature curves obtained from the thermocouples. To replicate the local time-temperature profiles, the thermophysical properties of the steel were experimentally determined and incorporated into a finite element analysis heat transfer simulation using Abaqus FEA® software. This simulation approach, combined with the MatCalc software, facilitated the calculation of various local microstructural characteristics such as carbide content, carbide type, carbide distribution, and chemical composition of the matrix. Furthermore, the content fractions of the microconstituents of the matrix, including martensite and retained austenite, were determined based on the simulated martensite start temperature, employing an optimized function fitted to experimental data. The developed simulation model offers potential applications in two important areas. Firstly, it can be used to adapt heat treatment processes for tools of different sizes in production, optimizing their mechanical properties. Secondly, it enables efficient optimization of heat treatment routes by considering changing initial states, leading to high process quality in terms of mechanical properties. Overall, this study provides valuable insights into the estimation and control of local microstructure in tool geometries through the use of a validated simulation model.

Keywords FEA · CALPHAD · Microstructural evolution · Tool steel · Optimization · Heat treatment

1 Introduction

High-quality tool steels are the backbone of our global production system: they give the desired shape to a host of other materials and produce parts of all sizes and geometries. According to Berns and Theisen [1], the typical properties of these tools are high mechanical strength, hardness, wear resistance, and sufficient toughness. In the case of tool steels, Hornbogen et al. [2] have shown that these properties are achieved by a multiphase microstructure that can be adjusted to the requirements of use through the manufacturing process,

chemical composition, and heat treatment. Bhadeshia and Honeycombe [3] pointed out that all components of the microstructure contribute to the obtained macroscopic properties. For a new industrial production tool, a complex parametric study is usually performed to obtain an optimal heat treatment route with the desired target properties for the product to be manufactured. The quenching temperature and the time in the industrial furnace are varied, followed by tempering heat treatments at a lower temperature to achieve the most efficient production possible. Typical austenitizing holding times, which increase with the thickness of the part, are in the range of 20 to 60 min. With the recent advancements in computer-aided material development and heat treatment simulation programs, ongoing efforts in science and industry aim to predict the required optimal microstructure and heat treatment using computer simulations, thus circumventing

✉ Jannik Schuppener
Schuppener@wtech.rub.de

¹ Chair of Materials Technology, Ruhr-University Bochum, Universitätsstraße 150, 44801 Bochum, Germany

the above-mentioned experimental parameter studies. As an example, Shubhank et al. [4] have developed a computer-aided simulation model in their application to predict the influence of heat treatment on low-alloy steels. Here, the approach was based on a fully automated quantitative image analysis. According to Eckstein [5], the tool geometry also significantly influences the necessary heat treatment parameters. Thin and small tools need significantly shorter holding times at hardening temperatures than similar tools with larger cross-sections for an identical material and furnace power. The differences in time-temperature curves between the core and the edge of the component are caused by the material's thermal conductivity and the heat transfer from the furnace to the tool. This can result in variations in the mechanical properties of the tool if the total holding time is insufficient.

In order to simulate the hardening/heat treatment process accurately, three interrelated variables must be calculated. Firstly, the model should precisely calculate the heat transfer from the industrial furnace into the component and the heat distribution within the component. This allows for the determination of real-time and temperature curves for any point in the tool. Secondly, the local microstructure needs to be calculated using these exact heat treatment processes, taking into account the initial state of the material (chemical composition, manufacturing route, etc.). Finally, an approach is required to determine the resulting mechanical properties from the local temperature-dependent microstructural changes, with the hardness of the material correlating with the start of the martensitic transformation (M_s temperature). In this paper, the microstructural evolution during heat treatment is studied and reproduced by a newly developed simulation model, thus developing the first two of the three interrelated variables. The martensitic transformation is a diffusionless transformation during quenching from supersaturated austenite to a tetragonal space-distorted lattice structure, which depends largely on the chemical composition of the austenite, as presented by Ishida [6] in their publication. According to Su et al. [7], the chemical composition of the austenite matrix is influenced

by the time- and temperature-dependent carbide dissolution during heat treatment. Several empirical equations have been established in the past to predict the onset of martensitic transformations as a function of the chemical composition of the material. Capdevila et al. [8] have recently developed an empirical equation for engineering steels through the use of an artificial neural network. A new equation to predict the M_s temperature in alloy steels was proposed by Lee and Park [9], which takes into account the effects of the chemical composition and grain size of austenite. These can be very well applied to low-alloy steels, in which the contained alloying elements are completely dissolved during austenitization. For higher-alloyed and multiphase tool steels, this underlying assumption is wrong, as part of the contained alloying elements is bound in the hard phases such as carbides.

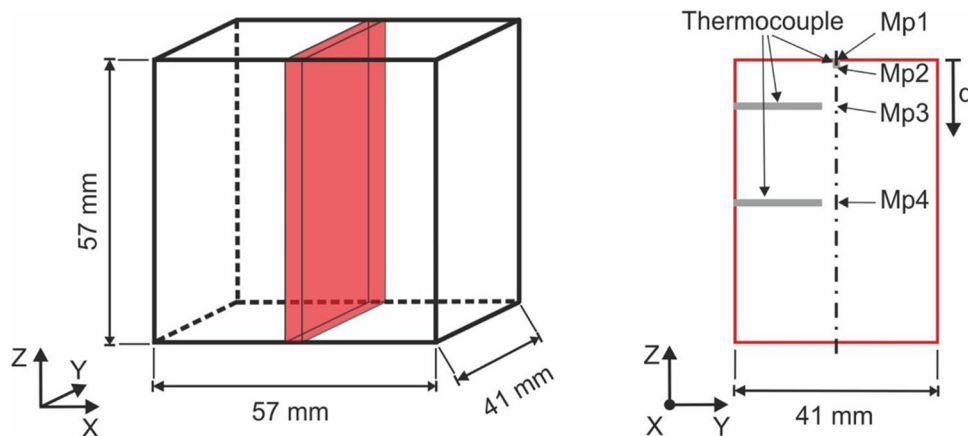
In this publication, the heat treatment of a metallic component is performed and its influence on the microstructure is studied. On the one hand, this heat treatment is carried out experimentally in a laboratory furnace (Section 2), and on the other hand, the same heat treatment is carried out in a simulation model (Section 3). The results of the experimental and simulated heat treatment are discussed comparatively in Section 4. Finally, Section 5 summarizes the findings and presents open questions and further developments.

2 Experimental

2.1 Sample geometry, material used, and measuring points investigated

In this work, a hot isostatically pressed powder metallurgy (PM-HIP) block with the dimensions $40 \times 50 \times 50$ mm (Fig. 1 left) made of the conventionally-available ledeburitic cold work steel 1.2379 (X153CrMoV12; AISI D2) was used as a replacement geometry for a tool, subjected to heat treatment and subsequently analyzed. The as-received condition was soft annealed. The chemical composition was analyzed by optical

Fig. 1 Schematic sketch of the examined PM block (left) with the cutout area shown (red) after heat treatment. On the right are the selected measuring points (Mp1-Mp4) for the mechanical and microstructural investigations and the holes for the temperature measurements with thermocouples in the PM block (gray)



spark emission spectrometry (OES) and the mean value from five individual measurements is shown in Table 1.

In the PM block, a total of four measuring regions were selected, which were investigated for their mechanical properties as well as their microstructure and their local time-temperature curve during heat treatment. All four measuring points examined are on the axis parallel to the z direction passing through the center of mass of the block, with increasing distance d to the edge (Fig. 1, right). The distances of the individual measuring points to the edge are shown in Table 2. The distance of 0.25 mm at Mp1 was selected as the minimum distance since the oxidation of the surface during heat treatment leads to a slight decarburization of the edge and thus changes the chemical composition. It is known from preliminary tests that at similar temperatures this decarburization of the edge is less than 0.15 mm and therefore at $d = 0.25$ mm an unchanged chemical composition can be assumed.

For the experimental determination of the M_s temperature, six cylindrical dilatometer specimens with a diameter of $D = 4$ mm and a length of $L = 10$ mm were made from the identical PM starting material.

2.2 Heat Treatment and temperature measurement

2.2.1 Furnace

The heat treatment of the PM block was carried out in a laboratory muffle furnace in an argon atmosphere followed by quenching in water. The austenitizing temperature was 1000 °C, and the sample was left in the furnace until the center of the component (Mp4) reached the austenitizing temperature of 1000 °C. This heat treatment was chosen to achieve the maximum possible hardness through the austenitizing temperature after quenching, and the comparatively short holding time was chosen to generate different properties at the edge and in the core. To ensure a uniform temperature distribution in the laboratory furnace, it was preheated to the austenitizing temperature for 3 h before the actual heat treatment of the PM block took place. To obtain an identical heat transfer from the furnace to all surfaces of the PM block, the block was placed in the furnace on two thin metallic residual pieces with a width of 2 mm, so that the underside of the block is only in negligible contact with a solid body.

In order to detect the temperature during the heat treatment in the component, holes with a diameter of 1.5 mm were drilled at the positions described in Fig. 1 right and Table 2. The depth of the hole drilled from the top surface to record the temperature curve of Mp2 is 2.5 mm, and the depth of both holes drilled from the side surface for Mp3 and Mp4 is 20 mm. The temperature was recorded during the heat treatment

Table 2 Distance d of the selected analysis area from the edge of the PM block (Fig. 1)

Measurement point	Mp1	Mp2	Mp3	Mp4
Distance (d) from the edge in mm	0.25	2.5	9.5	28.5

with a temperature data logger Voltkraft K204 with thermocouples of type K with a diameter of 1.5 mm. In addition, a thermocouple Tc1 was fixed on the surface of the PM block, and another thermocouple Tc0 was mounted 1 cm above the block to detect the exact furnace temperature. All thermocouples were connected to the PM block with a high-temperature stable molybdenum wire with a diameter of 1 mm (Fig. 2).

2.2.2 Quenching dilatometry

To measure the M_s temperature and to compare them with the results of the simulation, a quenching dilatometer DIL805 (TA Instruments, DE, USA) was used. The second derivative of the length change over the temperature was investigated to evaluate the dilatometer data. This allows the accurate determination of transformation points, by allowing large deviations from the zero line. Silica glass punches were used to measure the change in length of the samples under investigation, and K-type thermocouples with a diameter of 0.1 mm were welded to the surface of the dilatometer samples for temperature measurement and control. Due to the manufactured sample geometry of the PM block, the remaining piece was used to manufacture the dilatometer samples, resulting in a total of six samples. The initial condition of the dilatometer specimen must correspond to that of the PM block, which means that production from a different piece is not expedient. For sufficient statistics, three samples were needed for each heat treatment performed. Due to the low number of dilatometer samples, only the measuring points Mp2 (edge) and Mp4 (core) were considered here. In the dilatometer, the identical time and temperature curve of the measurement data of the furnace heat treatment of the PM block recorded by the temperature data logger was followed. To reduce oxidation, the tests were carried out under vacuum ($\sim 5 \cdot 10^{-4}$ mbar) and then quenched with nitrogen gas N_2 . Both time and temperature curves of the measuring points Mp2 and Mp4 were repeated and evaluated three times each.

2.3 Microscopy, phase analysis, and quantitative image analysis

The analysis of the microstructure as well as the quantitative image analysis of the different phases was carried out

Table 1 Chemical composition of the PM block (1.2379; AISI D2) determined by OES in wt%

Element	Fe	C	Si	Mn	P	S	Cr	Ni	Mo	Cu	V	W	Co
wt%	bal.	1.49	0.49	0.31	0.02	0.02	11.37	0.20	0.86	0.17	0.84	0.06	0.02

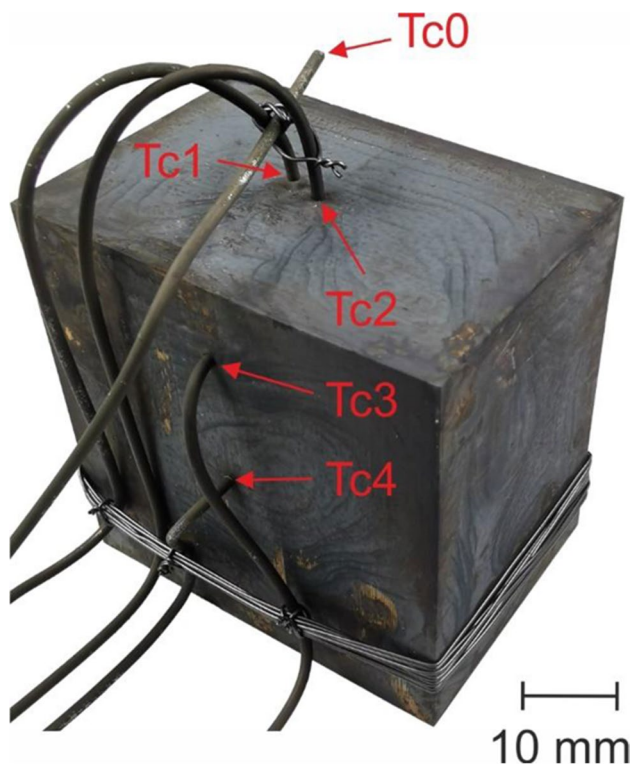


Fig. 2 PM block with type K thermocouples after heat treatment in the laboratory furnace

on metallographically prepared samples. For this purpose, a disc with a thickness of 4 mm was cut out of the center of the PM block (see Fig. 1). The disc was then further fragmented, and the measuring points Mp1-Mp3 together and Mp4 (center of the component) were individually hot embedded in conductive embedding material. Subsequently, the samples were metallographically ground and polished up to a 1 μm diamond suspension. For the exact quantitative phase analysis, the samples were observed in the polished state using a scanning electron microscope (SEM) of the type MIRA3 from TESCAN GmbH. An accelerating voltage of 15 kV, a working distance of 10 mm, and the BSE detector were used for imaging. Then, at the different distances from the edge of the PM block (Table 2), 132–140 single images were taken with a magnification of 15 kx and a square image side length of 18.4 μm . The brightness, contrast, and working distance between the different measuring positions were left constant. These individual images were then merged into a panorama image for each distance using the Fiji ImageJ2 1.52p software, and the gray value range was additionally matched to each other using histogram matching in ImageJ, validated in the study by Schindelin et al. [10]. This was done three times for each distance from the edge and three large high-resolution images ($>44,600 \mu\text{m}^2$) were evaluated for each measuring point (Mp1-Mp4) for quantitative image analysis.

A custom program developed by Benito et al. [11] was used in MATLAB® to perform a two-step semiautomatic segmentation of quantitative image analysis through gray level and feature size thresholding. The detected phases were characterized by their content, individual feature size, and shape, using area fraction, equivalent diameter, and aspect ratio as descriptors. These parameters were selected for compatibility with the input and output data of a later simulation model.

The phase identification was done using electron backscatter diffraction (EBSD) with 20 kV accelerating voltage and 17 mm working distance. The Nordlys Nano Detector and AZtec software from Oxford Instruments were utilized to conduct the EBSD scans, which were performed on tilted specimens at an angle of 70°. The identification of phases α -Fe, γ -Fe, M_7C_3 , MC, M_2C , and M_3C_2 was done using the inorganic crystal structure database (ICSD). The specimens were prepared with V2A etchant before the microstructural investigation.

2.4 Quantitative phase analysis and X-ray diffraction

The quantitative phase analysis was conducted using the PULSTEC μ -X360n mobile X-ray diffractometer, which uses Cr X-ray (CrK α radiation; $\lambda = 0.22898 \text{ nm}$) with 30 kV voltage and 1 mA current. The largest collimator (2 mm aperture) was used, and the X-ray exit-to-sample distance was $20 \pm 0.5 \text{ mm}$. An 18° beam entrance angle (ψ_0) resulted in an oval irradiated measurement range of $3.0 \times 2.8 \text{ mm}$ on the specimen. The X-ray diffraction (XRD) of the polycrystalline material formed Debye Scherrer rings, which were detected on the device's 2D photodiode detector. The XRD detected the diffraction of γ -iron (retained austenite, RA) in [220] orientation and α -iron in [211] orientation. According to the standard by [12] for X-ray determination of retained austenite the quantitative phase ratio between γ - and α -iron was calculated from the intensity curve areas of both phases. An average of at least five measurements was taken for each heat treatment, with a sample rotation of 50° between each measurement. The calculated retained austenite and martensite ratio is not equal to the real microstructure content because it does not account for the carbide content. The phase content of the carbides, determined by image analysis, was subtracted from the matrix content to determine the γ - and α -iron ratio. The RA content in vol. fraction was calculated using Eq. (1) that have been adapted on the approach of Su et al. [13].

$$RA = (1 - \text{Carbide}_{IA}) \cdot RA_{XRD} \quad (1)$$

where Carbide_{IA} is the carbide volume fraction measured by image analysis, and RA_{XRD} is the retained austenite volume fraction measured by XRD.

2.5 Hardness testing

The hardness of the metallographically prepared samples was measured using the Vickers method (DIN EN ISO 6507) in HV10. For each measuring point (Mp1-Mp4), a minimum of five individual measurements were carried out on a hardness tester from KB Prüftechnik GmbH, and the arithmetic mean and standard deviation were calculated. The measured hardness was added as an additional parameter in this work to represent the influence of different t-T profiles between the edge and core of the PM block on the microstructure and the resulting mechanical properties.

2.6 Thermophysical properties 1.2379-PM

The material's thermal conductivity λ was measured using the dynamic measurement method. By using this method, a differentiated measurement of the density ρ , specific isobar heat capacity c_p , and thermal diffusivity a as functions of temperature T was carried out. The resulting thermal conductivity is calculated using Eq. (2) [14].

$$\lambda(T) = \rho(T)c_p(T)a(T) \quad (2)$$

The density ρ_0 at room temperature was determined using Archimedes' principle. The corresponding measurements were performed in air and ethanol using a high-precision laboratory balance CPA225D by Sartorius AG. The thermal expansion coefficient was measured using a vertical dilatometer L75 Platinum series by Linseis Messgeraete GmbH. The specific isobar heat capacity c_p was measured using a differential scanning calorimeter type HDSC PT-1600 by Linseis Messgeraete GmbH, Selb, Germany. Measurements were performed immediately after baseline correction and calibration with a constant heating rate of 20 K/min.

To obtain the thermal diffusivity, laser-flash experiments were performed using a laser-flash analyzer type LFA 1250 by Linseis Messgeraete GmbH. The samples were prepared by coating them with a thin graphite layer to maximize the absorption of the laser.

3 Simulation model

The simulation model used to calculate the microstructure evolution consists of a combination of three major sub-steps and commercially available software packages. The simulation procedure is shown schematically in Fig. 3.

In the first step of the simulation, an optimization strategy was programmed in MATLAB® to calculate the heat transfer coefficient of the used laboratory furnace using the inverse method from the experimental t-T curves and an Abaqus FEA®

heat transfer analysis. In the next step, the Abaqus FEA® model with the optimized heat transfer coefficients was used to calculate the time and temperature curves as accurately as possible for each point of the component, considering the furnace- and thermophysical material parameters (Section 3.1). These local time and temperature curves are used as local heat treatment with the further material-specific input parameters of the initial state (chemical composition, carbide analysis) in MatCalc to calculate the metastable microstructure states and to simulate the M_s temperature and the resulting carbide distribution after the heat treatment (Section 3.2). The flowchart of the used simulation model in the MatCalc environment is shown in Fig. 4. Finally, with the output parameters from MatCalc and the optimized equation from an existing data set, the local matrix phase fraction (retained austenite content) can be calculated depending on the M_s temperature (Section 3.3).

3.1 Uncoupled thermal analysis of discontinuous interfaces

This Section briefly describes the mathematical relations assumed to describe the temperature evolution of the tool as it undergoes the heat treatment.

3.1.1 Heat conduction

The tool temperature distribution evolution is described by the heat conduction equation:

$$\rho c_p \frac{\partial T}{\partial t} = \nabla \cdot (\lambda \nabla T), \quad (3)$$

where t is the time and $\nabla \cdot$ and ∇ are the divergence and gradient operators, respectively. As detailed in Section 2.6, ρ , c_p , and λ are temperature-dependent.

The tool was given a homogeneous temperature as an initial condition:

$$T(t = 0) = T_0 \quad (4)$$

3.1.2 Boundary condition: interface heat transfer

Heat transfer within the furnace was modeled using the convective rule for interfaces as employed, for instance, by Schicchi et al. [15]:

$$-\lambda \frac{\partial T}{\partial x} = h_c \Delta T, \text{ with } \Delta T = T - T_F \neq 0, \quad (5)$$

where $T_F = T_F(t)$ is the time-dependent furnace environment temperature. $-\lambda \frac{\partial T}{\partial x} = q$ is the Fourier law of heat conduction, where q is the heat flux. h_c , on the other hand, is the heat transfer coefficient.

Fig. 3 Workflow of the entire microstructure simulation model

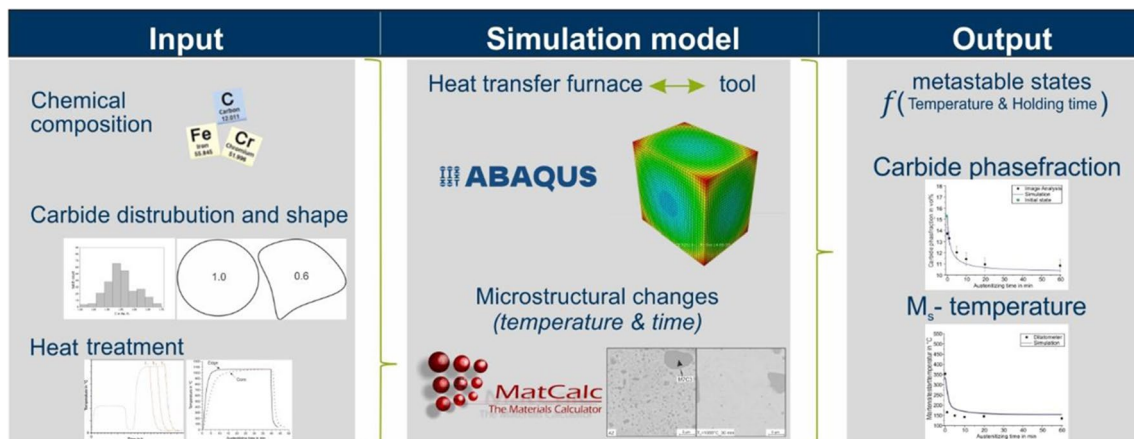
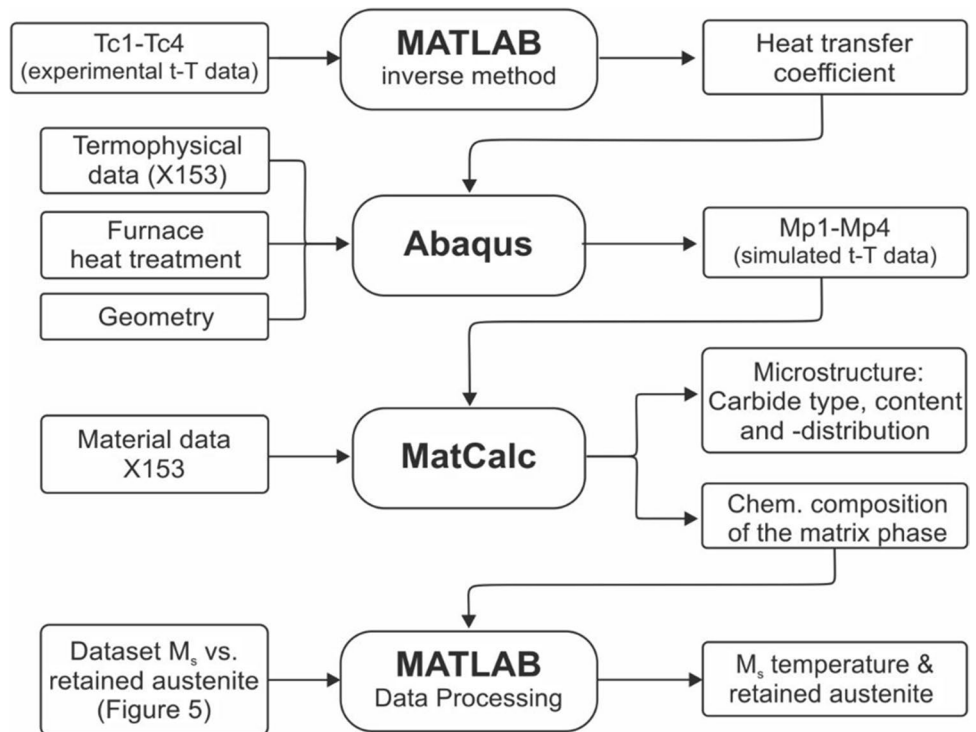


Fig. 4 Flow chart of the used simulation model in the MatCalc environment

3.1.3 Model construction

Abaqus/CAE® was used to create the geometric model with the same dimensions as the PM block (Fig. 2) and to set up the heat transfer from the laboratory furnace into the component as well as its time-dependent temperature distribution in the component. The general-purpose Abaqus/Standard® solver was employed as the finite element analysis (FEA) solver. In order to make the heat treatment simulation as faithful as possible to the experimental heat treatment, the experimentally determined time-temperature curves of the thermocouple Tc0 were used as the ambient temperature in the simulation. The results

of thermophysical properties as a function of temperature of 1.2379 PM were implemented as the material data.

3.1.4 Determination of the heat transfer coefficient between the laboratory furnace and component

The temperature-dependent heat transfer coefficient between the environment and the component depends on the furnace used, the proportions of convection and radiation, the surface structure of the component, etc. As mentioned above, since the value cannot be determined directly, it was determined by using the inverse method. The effectiveness of this approach

was demonstrated by Wu et al. [16] on samples of AlSi10Mg fabricated using selective laser melting, and by Xiong et al. [17] in the context of an inverse problem related to thermal engineering. For this purpose, the optimization function *fminsearch*nd written in MATLAB® and coded by D’Errico [18] was used. In this optimization function, the simplex search method is used to minimize the error between real measurement and simulation of the time-temperature curves of selected points. For this optimization, the measuring points of thermocouples Tc2, Tc3, and Tc4 were selected. The minimization function was defined as the sum of the integrated squared differences between the measured and simulated temperatures in Abaqus FEA® between a given start time *t_s* and the end of the simulation:

$$\arg \min_{h_c(T)} \sum_{i=2}^4 \int_{t_s}^{\infty} \sqrt{(T_{Tci}^{exp}(t) - T_{Tci}^{sim}(t))^2} dt \tag{6}$$

t_s is to be selected such that the emphasis of fitting through the inverse method is made on the Sections of the heat treatment that affect microstructural formation and evolution.

A temperature-dependent second-degree function Eq. (7) was assumed for the required heat transfer coefficient.

$$h_c(T) = a + b \cdot T + c \cdot T^2 \tag{7}$$

The bounds on the coefficients *a* and *b* were set as (0, ∞) to avoid negative heat transfer while retaining the capability to reproduce the expected behavior of *h_c(T)*.

3.2 Microstructure–MatCalc

The simulation of metastable microstructure was carried out using MatCalc Engineering 6.04 (rel.0.138) software, with the thermodynamic ME-Fe1.3.2 and the mobility ME-Fe1.2 database. MatCalc is a software package for simulating phase transformations, precipitation kinetics, and microstructure development in metallic systems. It uses the Onsager [19] thermodynamic extremal principle, which describes systems outside thermodynamic equilibrium. The simulation couples mathematical models to account for parallel processes in the material. In this work, kinetic calculations were used to dissociate carbides based on austenitizing time and temperature.

Thermodynamic equilibrium was determined by the minimum free enthalpy (G) of the system, using the CALPHAD method, which was extended with the SFFK model developed by Svoboda et al. [20] to predict precipitation growth rates and compositional changes. The GBB model published by Sonderegger and Kozeschnik [21] was used to model the interfacial energy of precipitates, while the NKW model from Kozeschnik et al. [22] calculated the evolution of precipitate size distribution. In this case, a class size of 25 was used. The simulation model considers the global chemical composition of the system from the OES analysis (Table 1). Precipitates extract elements from the matrix, conserving the total number of atoms per element, which is reflected in the SFFK model. Herrnring et al. [23] calculated the matrix chemical composition based on the elements “missing” due to the precipitates. The microstructure of the soft-annealed material was used as the starting point for the simulation. The required parameters for this initial state, such as the matrix phase, carbide types, contents, distribution, and shape, were determined through image analysis (Table 3). The Scheil-Gulliver solidification model shown by Schaffnit et al. [24] was used to calculate the chemical composition and amount of the eutectic M₇C₃-carbides and MC-phase. The proeutectoid and tempering carbides mean composition of the initial state was obtained from the thermodynamic equilibrium calculation at 860 °C, which represents a typical soft annealing temperature of 1.2379 shown in the data sheet by Stauberstahl [25].

The Abaqus FEA® heat transfer result as a time-temperature dataset for each node (equal to Mp1-Mp4) of Section 3.1 was used in the MatCalc simulation to determine carbide dissolution and evolving matrix composition based on temperature and time for each analyzed area. To calculate the M_s temperature, the empirical Eq. (8) by Barbier [26] and the chemical composition of the matrix phase (γ-iron austenite) were utilized.

$$M_s = 545 - 601.2 \cdot (1 - e^{-0.868 \cdot C}) - 34.4 \cdot \text{Mn} - 13.7 \cdot \text{Si} - 9.2 \cdot \text{Cr} - 17.3 \cdot \text{Ni} - 15.4 \cdot \text{Mo} + 10.8 \cdot \text{V} + 4.7 \cdot \text{Co} - 1.4 \cdot \text{Al} - 16.3 \cdot \text{Cu} - 361 \cdot \text{Nb} - 2.44 \cdot \text{Ti} - 3448 \cdot \text{B} \tag{8}$$

This described approach to the metastable microstructural evolution of carbide distribution, the carbide dissolution, and

Table 3 Results determined using image analysis. Input parameters and the initial state for the simulation

Phase	Phase fraction		Radius in μm				Aspect ratio
	vol%	*mol%	Mean	Std	Min	Max	Mean
M ₇ C ₃ (proeutectoid and temper)	12.31	14.48	0.30	0.28	0.08	1.18	0.75
M ₇ C ₃ (eutectic)	5.70	6.79	1.40	0.21	1.18	2.50	0.72
MC	0.09	0.11	0.05	0.02	0.01	0.08	0.86

*The contents in mol% were converted from the results of the image analysis (vol%) using the ThermoCalc 2023a software

the M_s temperature was successfully tested in previous work by Schuppener et al. [27] and improved by the new databases and optimizations.

3.3 Prediction of the retained austenite volume fraction

The computed M_s temperature was used to predict the retained austenite volume fraction after quenching, as it ultimately is a descriptor of the austenite phase stability. To achieve this, a dataset of the 30 pairs (M_s, V_{RA}) was acquired by dilatometry and XRD, respectively, for the studied material in a range of solution states. The austenitizing temperatures ranged between 980 and 1100 °C, and the holding times were between 1 and 60 min. The data is shown in Fig. 5. The selected model to describe the relation between V_{RA} and M_s was a three-parameter sigmoid function:

$$V_{RA}(M_s) = \frac{V_{RA}^{\min} - 1}{1 + \exp\left(\frac{(M_s - M_s^{RA50})}{k_{RA}}\right)} + 1 \quad (9)$$

where V_{RA}^{\min} is the retained austenite volume content at $M_s \gg 0$, M_s^{RA50} is the martensite start temperature at which the retained austenite volume fraction is 0.5, and k_{RA} indicates the sharpness of the transition. The fitting was performed in MATLAB® employing the Levenberg–Marquardt algorithm and minimizing the least absolute deviations. The fit, together with the 95% confidence bounds, is shown in Fig. 5 as well. The parameter values obtained, also with the 95% confidence bounds, are presented in Table 4.

4 Results and Discussion

The results and their discussion are divided into three sections. Section 4.1 discusses the microstructure and mechanical properties of the initial state, while Section 4.2 examines these properties following the heat treatment. Additionally, Section 4.2.2 compares and explains the differences between the simulated and experimental results. The main focus of the discussion is presented in Section 4.3, where the developed simulation model is compared and discussed in relation to other developed models.

4.1 Microstructure–initial state

The microstructure of the initial state is illustrated in Fig. 6 as an SEM image and it corresponds to a typical PM microstructure in the soft annealed state. Homogeneous

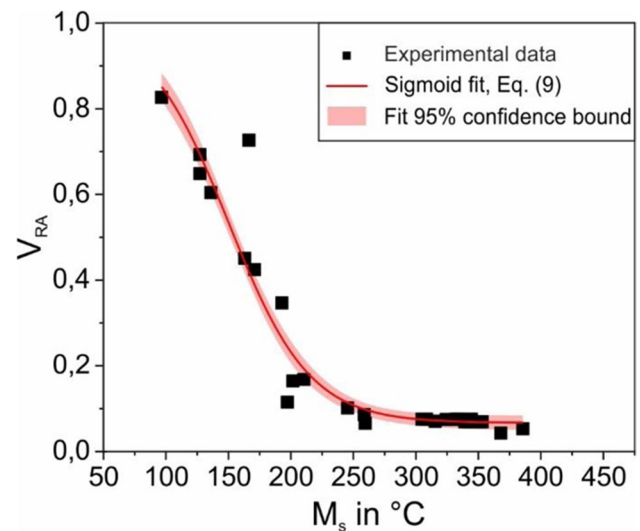


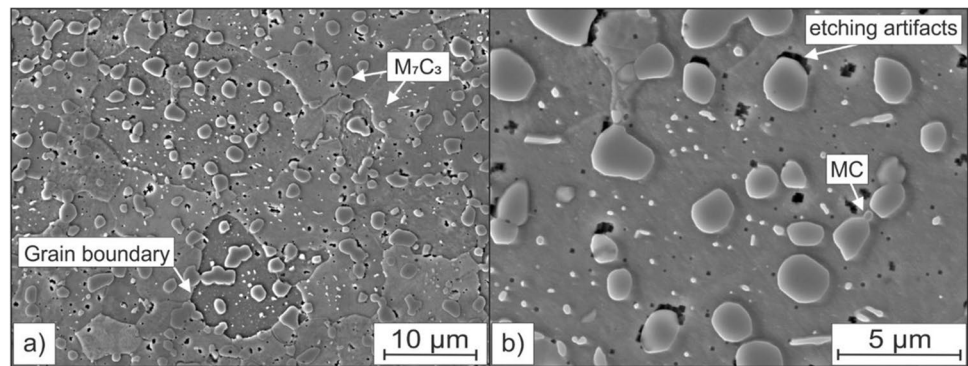
Fig. 5 Used data set for the calculation of the retained austenite volume fraction. Experimental results of the PM-Material as a function of M_s temperature after heat treatment in a dilatometer with varying austenitizing temperatures ($T_A = 980$ – 1100 °C) and holding times ($T_A = 1$ – 60 min)

Table 4 Fit parameters and confidence bounds of the Eq. (9)

Parameter	Value	95% confidence bound
V_{RA}^{\min}	0.0669	0.017
M_s^{RA50}	165.9	4.76
k_{RA}	38.58	4.5

distribution of larger round eutectic M_7C_3 carbides with a mean diameter of about 2.8 μm and a dispersed distribution of small secondary M_7C_3 carbides with a mean diameter of about 0.6 μm can be seen (Table 3). Using quantitative image analysis of the BSE panorama images (Section 2.3), a total content of approx. 18 vol.-% M_7C_3 carbides were determined. From the EBSD images shown in Fig. 7, a ferritic bcc structure was determined and a V-rich phase with fcc crystal structure in low volume contents (0.09 vol.-%) could be detected, which is labeled as the VC phase. Figure 8 displays the results of the thermodynamic simulation ($T = 500$ – 1450 °C) with the Software MatCalc. Although this VC phase is not thermodynamically stable at the conventional soft annealing temperature of $T_{\text{soft}} = 860$ °C (Fig. 8b), a content of approx. 0.17 vol.-% VC can arise during solidification due to segregation (Fig. 8a) and could remain in the microstructure after soft annealing. In this condition, the material has a hardness of approx. 223 ± 8 HV10.

Fig. 6 SEM microscope images of the microstructure of the PM block in its initial state. Etched condition, recorded using secondary electrons (SE) contrast with **a)** 5.000× and 15.000× magnification (**b)**



4.2 Microstructure and mechanical properties after the heat treatment

4.2.1 Heat treatment in the Laboratory furnace—experimental execution

The temperature data of the laboratory furnace measured by the temperature data logger and the total of four measuring positions in the PM block are shown in Fig. 9. The furnace temperature Tc0 rose quickly to a temperature of approx. 930 °C after roughly 70 s and then continued to rise to a temperature of approx. 950 °C up to a holding time of 200 s. When the laboratory furnace was opened, the temperature dropped from the preheated temperature $T = 1000$ to 930 °C. Due to the inertia of the comparatively thick thermocouples of approx. 1.5 mm, a too-low ambient temperature was indicated by the temperature data logger at the beginning. Similar correlations were observed, for example, in the study

of Wiegand [28] and this correlation is also described in the associated standard by Deutsche Norm [29]. The largest temperature differences were found between the thermocouples Tc2-Tc4 at the beginning of the heat treatment. After a holding time of approximately 950 s, the temperature difference between Tc2 (2.5 mm) and Tc4 (28.5 mm) was only 4 °C, eventually reaching the same temperature of $T = 982$ °C at $t = 1050$ s. After approximately 1200 s of heating, a nearly homogeneous temperature of 1000 °C was achieved throughout the entire tool, which was subsequently quenched in water. A temporary temperature plateau at a temperature of approximately 820 °C can also be observed. The reason for this plateau is the material-specific thermal conductivity, which has local minima in the temperature range of the phase transformation from bcc to fcc (Fig. 10) and the temperature can be transferred much more poorly. Furthermore, the specific heat capacity (Fig. 10b) explains this phenomenon. Due to the phase transformation, more

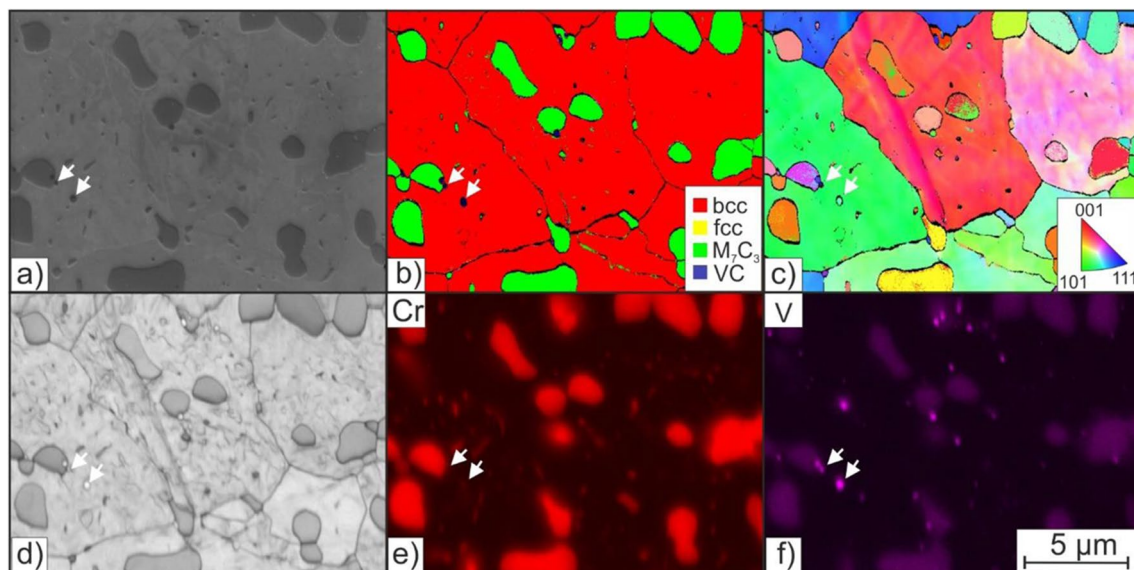


Fig. 7 EBSD images of the PM block in its initial state and polished condition. SE contrast (**a**), phase distribution map (**b**), inverse pole figure (IPF-X) (**c**), band contrast (**d**), and qualitative element map of Cr- (**e**) and V-fraction (**f**)

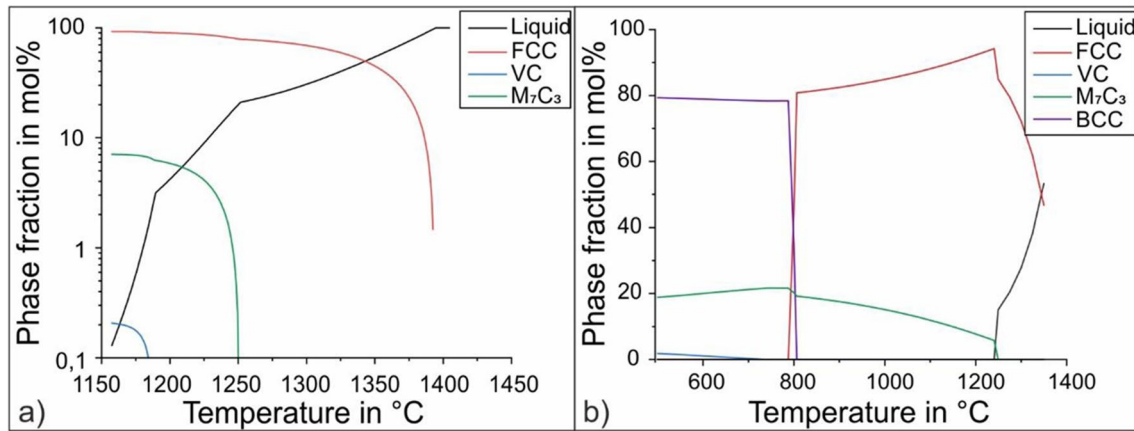


Fig. 8 Results of the thermodynamic simulation with the Software MatCalc. Scheil-Gulliver simulation (a) and thermodynamic equilibrium calculation with the CALPHAD method (b)

energy is required to change the internal energy of the system, resulting in a sharp increase in the specific heat capacity. This results from the latent heat required for the bcc to the fcc transformation.

Figure 11 shows exemplarily the microstructure after heat treatment in the laboratory furnace at Mp2. Figure 12, on the other hand, shows EBSD data of the same position. Only one instance is shown because the differences between positions cannot be assessed qualitatively through simple visual inspection. Instead, an in-depth quantitative image analysis as described in Section 2.3 was pursued. Therefore, only the SEM images of the measuring area Mp2 are presented in this part and the other measuring areas (edge-core) are discussed by extended measurement data. A martensitic structure can be seen, which, according to Krauss and

Marder [30] martensite morphology studies, can be assigned to the plate martensite. Also, the round, non-dissolved, and evenly distributed M₇C₃ carbides can be seen. Due to the low chosen austenitizing temperature and relatively short chosen heat treatment time, only a small amount of the C-containing carbides dissolves. The dissolved C-content in the matrix can be estimated from the martensite morphology (plate martensite). For low-alloy martensitic steels, this is $C < 0.5$ vol% which can be compared with the following simulations results. In the EBSD images (Fig. 12b), retained austenite (yellow) and undissolved VC carbides (blue) were detected after heat treatment in all examined areas. The shift of both M_s and martensite finish (M_f) temperatures to lower values as a result of the enrichment of the matrix with alloying elements is noteworthy. When the M_f temperature falls below the quenching temperature of 25 °C, the martensitic transformation becomes incomplete, and some austenite persists in the microstructure as retained austenite, which has been shown in the works of Berns and Theisen [1]. This can be seen in the EBDS images between the martensitic plates (yellow). The retained austenite contents detected by EBSD are lower compared to the values determined by X-ray photography, as the areas with high dislocation density with EBSD lead to poor or no Kikuchi patterns. Brodusch et al. [31] have already investigated the impact of high dislocation density on phase determination, which poses a challenge in this regard.

The remaining VC carbides are conspicuous in the microstructure after heat treatment. The presence of the VC carbides in the initial state was previously explained. With the heat treatment carried out at a temperature > 750 °C, this VC phase is no longer thermodynamically stable (Fig. 8b) and should dissolve. However, a small amount of approx. 0.1 vol% remains in the microstructure after quenching. One possible explanation could be insufficient time for a

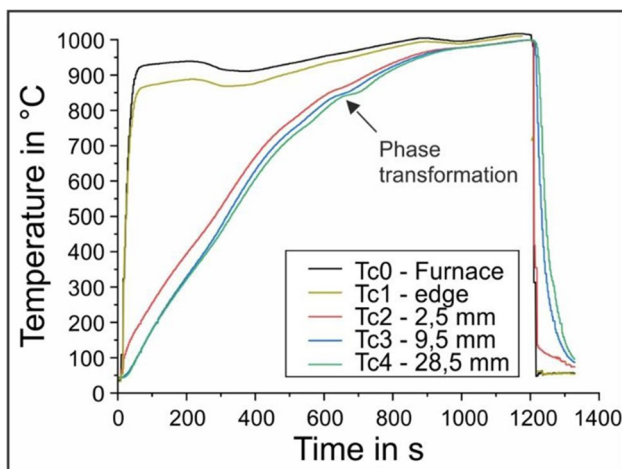


Fig. 9 Time-temperature measurements during the heat treatment of the PM block using type K thermocouples in the laboratory furnace (Fig. 2)

Fig. 10 Results of the thermo-physical properties as a function of the temperature of the 1.2379 PM and required material data for the Abaqus simulation: density (a), specific heat capacity (b), thermal diffusivity (c), and the thermal conductivity (d) calculated from the values mentioned previously

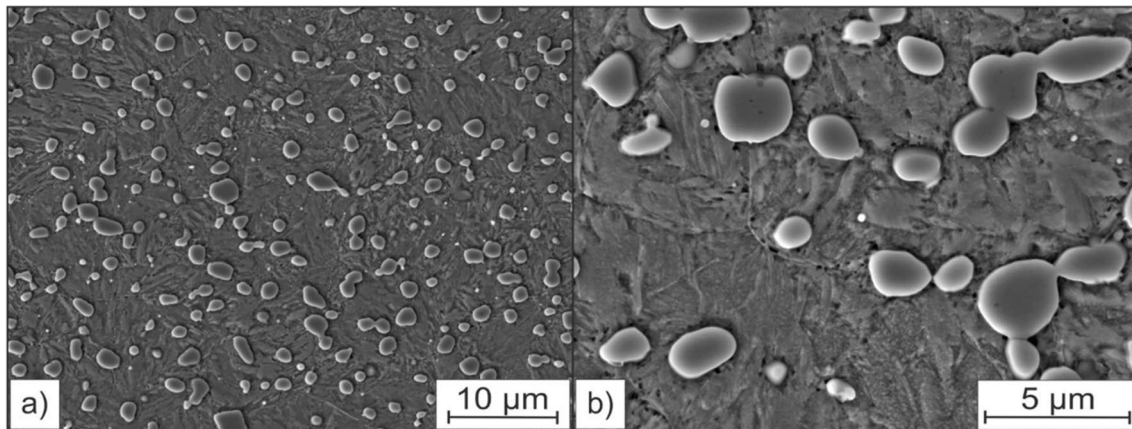
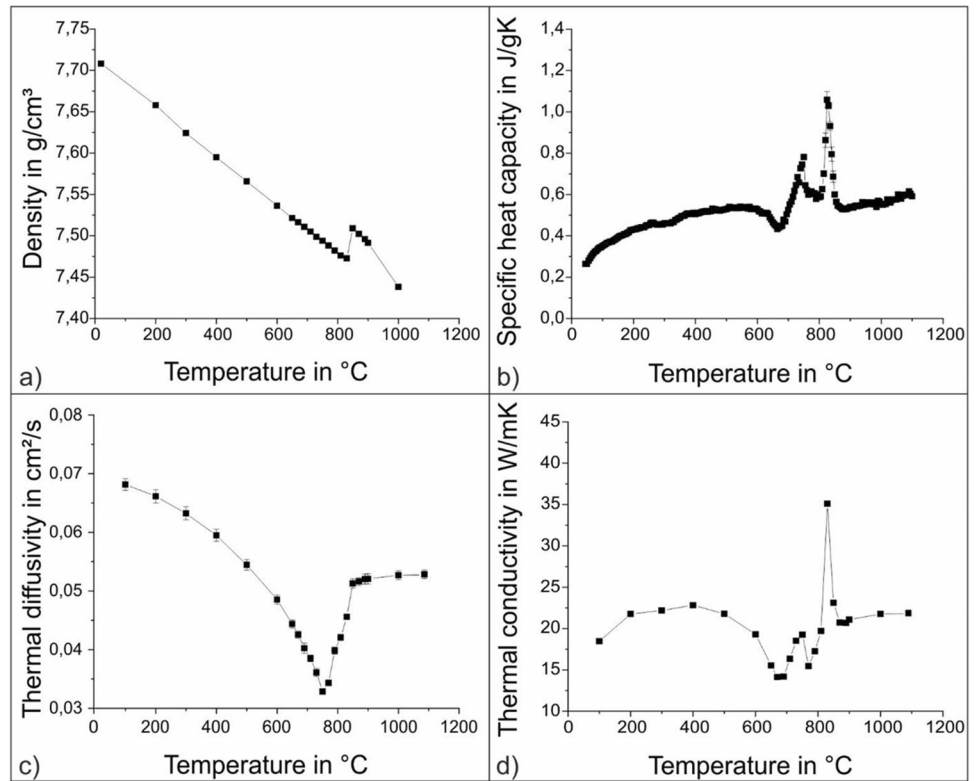


Fig. 11 SEM microscope images of the microstructure of the block (Mp2) after the heat treatment in the laboratory furnace. Etched state, recorded using SE contrast with 5.000× (a) and 15.000× (b) magnification

complete dissolution of the VC carbides. By prolonging the holding time, complete dissolution of the VC carbides may be achieved. On the other hand, it is noticeable that the VC carbides are increasingly located on the interfaces of the M_7C_3 carbides or are even completely surrounded by them (EBSD Figs. 7 and 12). These contact areas can lead to a mutual influence of the diffusible dissolution kinetics. The enrichment of the interface with alloying elements from the dissolving carbides creates a local concentration maximum, which counteracts the further dissolution of the carbides and

increases the heat treatment time required for a complete dissolution.

Figure 13 presents the comprehensive results of all analyzed areas (Mp1-Mp4). Note that the simulation results are further discussed in the Section 4.2.2. By utilizing quantitative image analysis, even subtle variations in the carbide content of these areas could be detected. The M_7C_3 carbide content after the heat treatment of the PM block is approximately 14.6 vol.-% at the edge, which increases to 15.2 vol.-% towards the center of the component. The locally

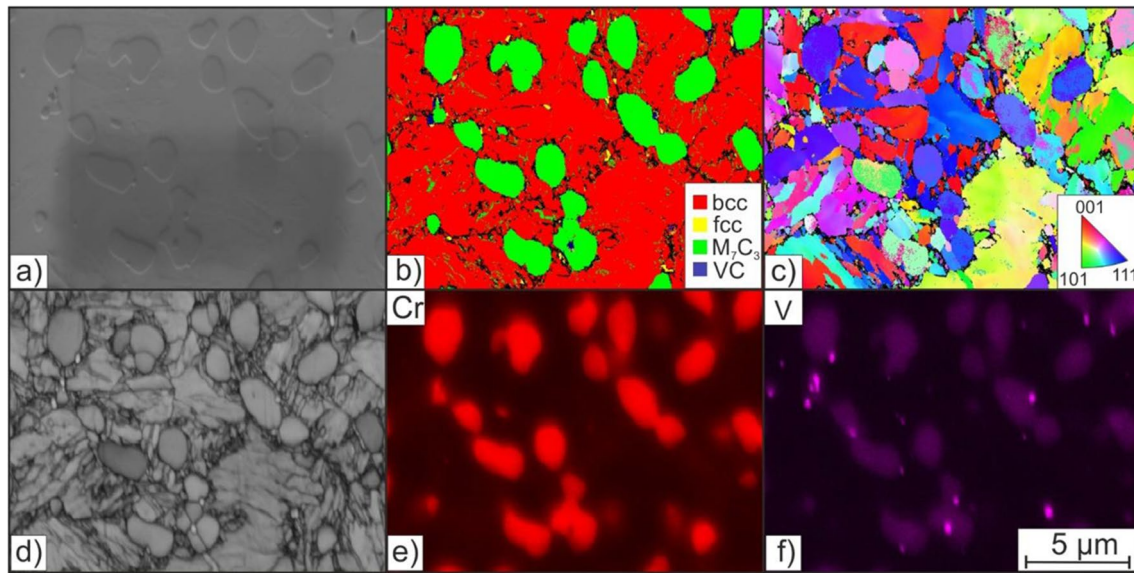


Fig. 12 EBSD images of the PM block (Mp2) after the heat treatment and in a polished condition. SE contrast (a), phase distribution map (b), inverse pole figure (IPF-X) (c), band contrast (d), and qualitative element map of Cr- (e) and V-fraction (f)

deviating time and temperature curves (Fig. 9) result in the edge of the PM block (Mp1) reaching the transformation temperature range of approximately 820 °C earlier than the core of the part. Consequently, with the locally increasing temperature, the thermodynamically stable phase content of the M_7C_3 carbides decreases. At the austenitizing temperature of 1000 °C, the thermodynamic equilibrium content of M_7C_3 carbide for this material is 13.5 vol.-% (Fig. 8). Hence, the carbides dissolve by the chemical driving force, with dissolution initiating first in the edge region of the PM block. Gottstein [32] extensively demonstrated in his work that the rate of carbide dissolution is dependent on several factors, including the material's temperature, the holding time, and the thermodynamic driving force from the initial state to the thermodynamic equilibrium.

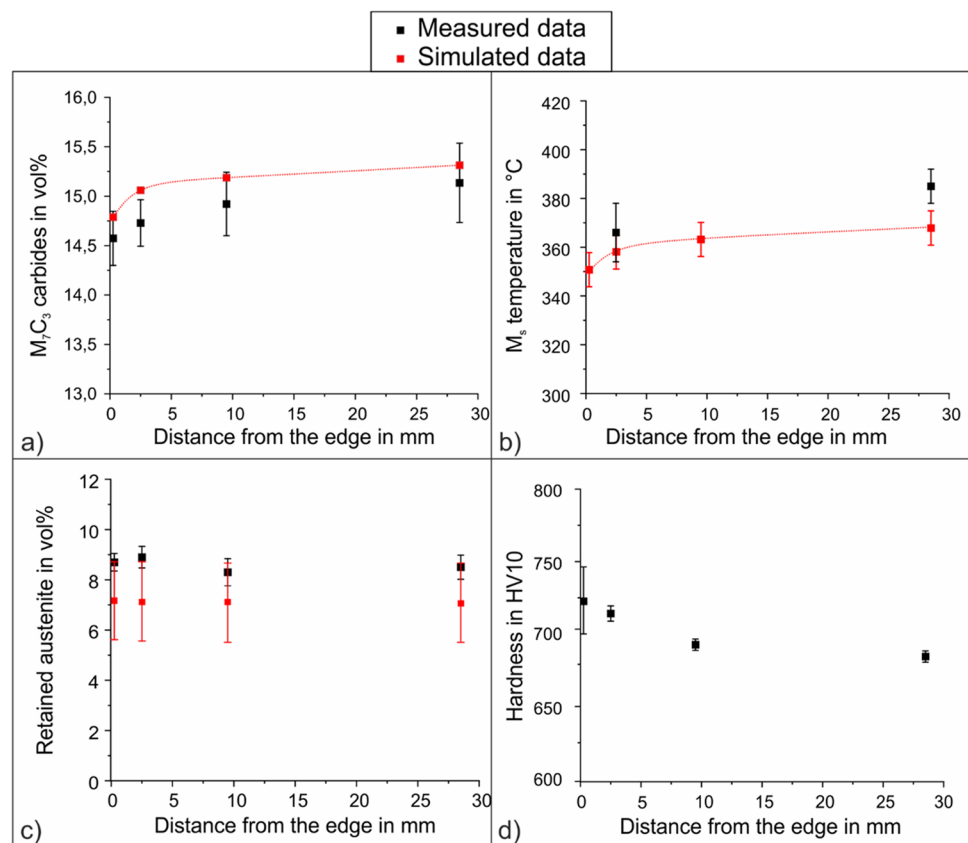
Due to the dissolution of the carbides, the matrix is enriched with the carbide-forming alloying elements. In the case of the carbides M_7C_3 and VC, these are mainly the alloying elements C, Cr, and V. Due to the higher content of these alloying elements in the matrix, the martensitic transformation is shifted to lower temperatures, and M_s temperature drops. This relationship was observed by Platl et al. [33] for tool steels and by Peet [34], among others. This also correlates with the results of the dilatometric evaluation. The time-temperature history of the edge area (Mp2; $d = 0.25$ mm) reaches a lower M_s temperature of $M_{s(Mp2)} = 366 \pm 12$ °C as the time-temperature curve of the component center (Mp4; $d = 28.5$ mm) with a M_s temperature of $M_{s(Mp4)} = 385 \pm 7$ °C (Fig. 13b).

Based on Qiao et al. [35] through the enrichment of the matrix with alloying elements and the resulting

decrease in the M_s temperature, the retained austenite detected in Fig. 12 remains in the microstructure. After the heat treatment in the laboratory furnace, a retained austenite content of 8.9 vol.-% is measured by X-ray diffraction (Section 2.4) in the edge area, and a retained austenite content of 8.5 vol.-% in the core of the PM block (Fig. 13d).

The local hardness of the PM block is determined by the collective contribution of individual phase properties explained by Berns [36]. The heterogeneous time-temperature profiles during the heat treatment of the edge of the PM block leads to a higher dissolution of carbides, which consequently enriches the matrix with alloying elements. This process results in a lower M_s temperature and a delay in the diffusion-controlled pearlite transformation. As a result, a complete, diffusionless martensitic transformation occurs. The hardness of the martensitic structure is directly proportional to the dissolved C-content and increases with the lattice distortion caused by the higher C-content. This relationship was recently reaffirmed by Damon et al. [37] for a PM-steel Astaloy 85Mo. M_7C_3 carbides contain 30 at.% and VC carbides even up to 50 at.% carbon, which is included in the matrix by the dissolution of the carbides. Due to the higher carbide solution in the edge than in the core, the PM block reaches a hardness of 720 HV10, which decreases to a hardness of 675 HV10 in the center of the component. The observed enrichment of the matrix with alloying elements, as a result of differential carbide dissolution, exhibits a strong correlation with the resulting hardness of the material after heat treatment.

Fig. 13 Comparison of the experimental with the simulation results after the heat treatment of the PM block. Phase fraction* of the M_7C_3 carbides (a), martensite start temperature (b), retained austenite fraction (c), and hardness (d). (*) The contents of M_7C_3 carbides in vol% were converted from the results of the MatCalc simulation (mol%) using the ThermoCalc 2023a software



4.2.2 Simulation of the microstructure-simulative execution

Heat transfer Figure 10 illustrates the temperature-dependent thermophysical properties of the analyzed material 1.2379, which constitute crucial material data for conducting the heat transfer simulation. Figure 14 a presents a graphical representation of the temperature-dependent heat transfer coefficients that have been optimized by the inverse method for the side, top, and bottom surfaces. Ko [38] observed the increase in heat transfer is attributed to the overlapping effects of convection and thermal radiation, which become more significant at higher temperatures. Moreover, the heat input through the side surfaces is notably higher compared to the top and bottom surfaces. This observation aligns with the actual experimental setup as the heating elements of the laboratory furnace are also attached only to the sides and not to the upper and lower surfaces.

In Fig. 14b the temperature difference ΔT at Mp2-Mp4 between the data measured using thermocouples and the simulated temperature (using the results of the inverse method) during the heat treatment carried out is illustrated. While at the beginning of the heat treatment, there is still a considerable deviation of ± 30 °C between the experimental performance and the simulation of the temperature, from a heat treatment time of $t > 650$ s onwards, only minor

differences were detected. This behavior is expected, as the fitting start time t_s of Eq. (6) in the Section 3.1.4 was set to 650 s, since the austenitic transformation and thus also the carbide dissolution begins approx. at that heat treatment time ($T > 820$ °C, $t > 650$ s; Fig. 9), the slightly deviating start of the simulation and its ΔT to the experiments has no major influence on the simulation result.

Microstructure The primary objective of constructing this simulation model is to predict the microstructure resulting from diverse furnace settings, heat treatment parameters, and geometries using the 1.2379 cold work tool steel. The comparison between the experimental and simulation findings after the PM block's heat treatment is presented in Fig. 13(a) shows phase fraction of the M_7C_3 carbides, (b) displays the martensite start temperature, and (c) the retained austenite fraction.

The dissolution behavior of carbides could be accurately simulated as a function of the initial conditions and heat treatment. However, there are slight discrepancies between the calculated M_7C_3 carbide contents using the MatCalc simulation and those determined by quantitative image analysis, with slightly higher carbide contents (0.2–0.35 vol%) calculated by the simulation. These differences may be attributed to challenges in the image analysis process, where even small variations in the thresholding segmentation settings

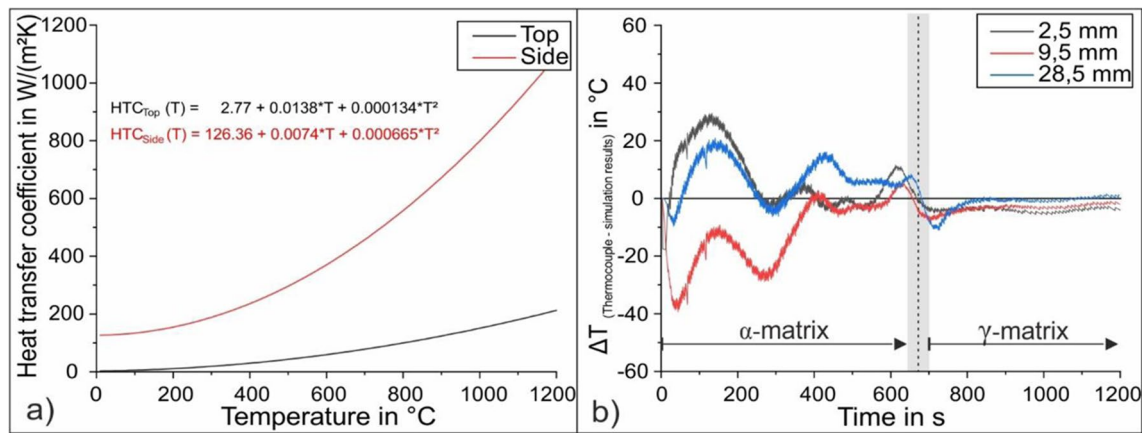


Fig. 14 Simulation results of the inverse method. Optimized function of the heat transfer coefficient for the upper surface and the side surface as a function of temperature (a) and temperature difference ΔT

at Mp2–Mp4 between the data measured using thermocouples and the simulated temperature during the heat treatment carried out (b)

can lead to higher or lower detected phase contents. The difficulties with image analysis of the initial state have been previously described and discussed in the work by Schuppener et al. [27] which validated the method for the simulation of metastable microstructure states. The simulation of carbide dissolution results in an enrichment of the matrix with its alloying elements. Table 5 displays the simulated chemical composition of the matrix phase using MatCalc software.

Using the chemical composition of the matrix and Eq. (8), the M_s temperature was calculated and presented in Fig. 13b. The simulated M_s temperature was found to be lower by approximately 10–20 $^{\circ}C$ compared to the experimental values obtained through dilatometry. This can be attributed to the higher simulated carbide content, leading to a lower matrix potential, which should theoretically result in a higher simulated M_s temperature than experimentally determined. It is worth noting that the empirical equation used to calculate M_s as a function of dissolved alloying elements is based on experimental data and does not replicate the actual martensitic transformation mechanism. Furthermore, this equation was developed from a large data set of different martensitic material groups to accurately represent as wide a range as possible. Due to the data fit, a slight deviation may be present in the calculation of M_s .

The simulation model calculated the retained austenite content as a function of the M_s temperature, using an experimental data set (Section 3.3). Figure 13c compares the simulated contents to the experimentally determined values using XRD. The simulated M_s temperatures resulted in a retained austenite content of approximately 7.2 ± 1.6 vol% in the edge area and 7.0 ± 1.6 vol% in the core of the PM block. The simulated values were found to be about 1% lower than the experimentally determined values, but the quantitative determination of retained austenite by XRD is accompanied by a slight inaccuracy at low contents. Additionally, the experimentally determined values fell within the 95% confidence bounds of the simulation results, indicating a satisfactory agreement between the two.

4.3 Exploring the potential of the simulation model: comparing alternative methods for predicting the microstructure

In order to simulate the heat treatment and resulting microstructure, various approaches and publications have been developed and will be compared to the simulation model created and validated in this study and previous publications by the authors Schuppener et al. [27].

Table 5 Chemical composition in wt% of the matrix phase at the measurement points Mp1–Mp4. Calculated with the simulation model

Measurement point	Fe	C	Mn	Si	Cr	Ni	Mo	V	Co	Cu
Mp1	bal.	0,26	0,32	0,58	4,43	0,23	0,36	0,17	0,02	0,20
Mp2	bal.	0,25	0,32	0,58	4,38	0,23	0,36	0,16	0,02	0,20
Mp3	bal.	0,24	0,32	0,58	4,35	0,23	0,36	0,16	0,02	0,20
Mp4	bal.	0,23	0,32	0,58	4,33	0,23	0,36	0,16	0,02	0,20

The used hardening temperature is a significant parameter in the heat treatment process. In materials presenting martensitic transformations, the objective of the hardening temperature is to dissolve a certain amount of carbides present to achieve the desired matrix potential for martensitic hardness or to dissolve enough alloying elements capable of forming tempering carbides for high-temperature applications. Both variants can be adjusted and correlated using the M_s temperature. To rapidly estimate the M_s temperature of low to medium alloyed martensitic steels, one option is to employ an appropriate empirical equation such as the one proposed by Ishida [6], which utilizes the chemical composition of the matrix. More details on this approach can be found in Section 3.2. The CALPHAD method is another viable option for calculating the required hardening temperature. For low-alloyed martensitic materials ($C < 0,7$ mass%), a hardening temperature is required, at which all existing carbides dissolve and result in a single-phase austenitic state prior to quenching that has been shown in the work on high carbon martensite by Mola and Ren [39]. This produces a matrix composition that is equal to the steel's global chemical composition. Numerous applications utilize this method to calculate the martensitic transformation and ultimately determine the microstructure from the hardening temperature. However, this approach can only be applied if obtaining a complete solution of all carbides before quenching is desirable.

Hence, the described method is not suitable for high-alloy tool steels, since the microstructure in the application typically consists of a multiphase system. A complete dissolution or an excessive amount of dissolved carbides can lead to significantly increased retained austenite contents after quenching. This results in an unsuitable microstructure for the application due to poorer mechanical properties. A corresponding hardening temperature must be calculated, in which a defined amount of carbides dissolve and the matrix composition attains the appropriate matrix potential for the intended application. In order to predict the M_s temperature of high-alloyed tool steels, many publications describe the composition of the austenite through thermodynamic calculations. For example, this approach has been used by Bhadeshia [40] for substitutionally alloyed steels, and Hanumantharaju [41] has employed this approach for thermodynamic modeling of the martensite start temperature in 1500 commercial and novel alloys. With this approach, the authors obtain a matrix potential as a function of the calculated hardening temperature. The accuracy of the calculated results depends decisively on the quality of the database used, which is constantly expanded and improved by experimental measurements by Thermo-Calc, JMatPro, and other providers.

These two described approaches for the calculation of the martensite start temperature have however the crucial

disadvantage that with the CALPHAD method, only a thermodynamic equilibrium is calculated. This state is reached after an infinitely long holding time, which is not the case in technical heat treatments. According to Kroupa [42] through the use of the CALPHAD method, the required heat treatment time is not really considered in these approaches.

As mentioned above, the required holding time is influenced by the initial condition and its manufacturing route. This initial state and the resulting required heat treatment time can be considered by using the software MatCalc (Section 3.2). This software package is designed to simulate the precipitation kinetics that take place during a range of metallurgical processes, using thermo-kinetic modeling techniques that have been investigated by Kozeschnik and Buchmayr [43]. The software employs a CALPHAD-type database, an approach used to perform thermodynamic and kinetic calculations in systems consisting of multiple components Nayak et al. [44]. By employing this approach, the metastable microstructural states resulting from technically feasible heat treatment times can be calculated for carbide dissolution during austenitizing. This method has been previously explored for various martensitic systems and has demonstrated favorable agreement between the simulated and experimentally determined microstructure and M_s temperature, which could also be observed in this publication. Schuppener et al. [27] have used this method for the simulation of the cold work tool steel X153CrMoV12 and Schmidtseifer and Weber [45] validated this method on the martensitic stainless steel X20Cr13.

Nonetheless, this overall technique lacked a link to real tool geometry and heat treatment in an industrial furnace. In this study, we established this connection by using experimentally determined thermophysical data for the used material, furnace-specific heat transfer coefficients determined by the inverse method and FEA software, and significantly improves the simulation, allowing it to be applied to real tools and heat treatment furnaces. With this approach, it is now possible to simulate and optimize the metastable microstructure of any tool geometry after any given hardening process, reducing the experimental effort substantially. The use of digital workflows in steel heat treatment is gaining significance in the context of integrated computational materials engineering as it provides a more precise estimation of the microstructure, hardness, strength, residual stress, and deformation of workpieces. Specifically, several research studies have been conducted to simulate the austenitization and quenching processes involved. However, these simulations such as by Moumni et al. [46] focus on the diffusion-driven phase formation during cooling and the resulting phases consisting of martensite, pearlite, bainite, and ferrite or the distortion of this phase transformation of the tool which have been shown by Simsir et al. [47]. Again, the resulting properties such as residual stress after austenitizing

and quenching result from the phase mixtures and thermal quenching curves. However, all these publications assume a homogeneous initial state before quenching.

The connection between thermo-kinetic simulations in MatCalc and finite element analysis of heat transfer using Abaqus was seldom explored up until now. However, by Eser et al. [48, 49] have utilized this combination of methods to simulate local microstructure, mechanical property evolution, and resulting residual stresses during the tempering process of AISI H13 steel. Nevertheless, it should be noted that the simulation model employed by Eser et al. does also assume of a homogeneous microstructure before quenching. This limitation may affect the accuracy of the simulation results, as demonstrated in this study, where metastable heat treatments resulted in differences in the local microstructure between the edge and core of the tool bevor and therefore after quenching.

5 Conclusion and outlook

The developed simulation model shows a promising potential for applications in two key areas for adapting heat treatment for tools in real production processes and accounting for changing initial states.

Firstly, it can be used to simulate a computer-controlled heat treatment for a new product geometry which can significantly reduce the parameter matrix required to develop or optimize an efficient heat treatment route. Typically, this involves determining the hardening temperature and holding time, followed by tempering heat treatment. Additionally, the model presented here enables the estimation of different local mechanical properties at the component edge and core, which result from deviations in holding times and cooling rates between the two regions in an industrial heat treatment furnace. The potential applications of the simulation model have been demonstrated through experimental and simulation results presented in this work.

Secondly, the simulation model can be used to optimize the heat treatment for the present batch composition. Slight variations in the chemical composition of the initial materials are present during the manufacture of tools and metallic production tracks. Currently, changes in composition are not considered during production, and the heat treatment route developed previously for the same material is usually not altered. As an example, in an industrial heat treatment with the usage of a continuous furnace, it is easy to vary the holding time by changing the conveyor speed, thereby adapting the heat treatment to the actual batch condition. The aim is to achieve a holding time at which the chemical composition of the austenite prior to quenching is identical, so that after quenching, a constant ratio of the phases contained and thus,

constant mechanical properties can be achieved to a very good approximation.

With the workflow presented, it is possible to calculate the local microstructure of the 1.2379 for any geometry and heat treatment temperature in any furnace after quenching, exhibiting a broad and extensive range of applications. A good agreement between simulation and experiment was achieved. The small differences in the carbide content can be explained by the challenges in the use of quantitative image analysis. The prediction of M_s temperature with an empirical equation and the simulated chemical composition of the matrix with MatCalc in the investigated area leads to a modest underestimate of the M_s temperature. Furthermore, the developed approach to calculate the retained austenite content achieves sufficient accuracy in the simulation used. The next step in the ongoing development of the simulation model is to develop a scientific approach to calculating the mechanical properties from the simulated phase fractions and composition.

The used simulation model can be adapted for industrial heat treatment furnaces with little effort. Only the determination of the heat transfer coefficient is required. In addition, the developed simulation model can be adapted to other carbide-containing cold work steels.

Acknowledgements The authors would like to express their gratitude to Dörrenberg Edelmetall GmbH for generously providing the PM material 1.2379 used in the development and validation of the simulation model used in this study. The simulations and investigations were performed at the Ruhr-Universität Bochum (Bochum, Germany) within the research project “KnowDiPro” funded by Arnsberg District Government as part of the Progres.NRW (ref. no. 3326010031).

Author contributions All authors contributed to the study conception and design. Material preparation, data collection, and analysis were performed by Jannik Schuppener, Aaron Berger, and Santiago Benito. The first draft of the manuscript was written by Jannik Schuppener, and all authors commented on previous versions of the manuscript. All authors read and approved the final manuscript.

Funding Open Access funding enabled and organized by Projekt DEAL. The simulations and investigations were performed at Ruhr-Universität Bochum (Bochum, Germany) within the research project “KnowDiPro” funded by Arnsberg District Government as part of the Progres.NRW (ref. no. 3326010031).

Declarations

Competing interest The authors declare no competing interests.

Open Access This article is licensed under a Creative Commons Attribution 4.0 International License, which permits use, sharing, adaptation, distribution and reproduction in any medium or format, as long as you give appropriate credit to the original author(s) and the source, provide a link to the Creative Commons licence, and indicate if changes were made. The images or other third party material in this article are included in the article's Creative Commons licence, unless indicated otherwise in a credit line to the material. If material is not included in the article's Creative Commons licence and your intended use is not

permitted by statutory regulation or exceeds the permitted use, you will need to obtain permission directly from the copyright holder. To view a copy of this licence, visit <http://creativecommons.org/licenses/by/4.0/>.

References

- Berns H, Theisen W (2008) Ferrous materials: steel and cast iron. Springer, Berlin/Heidelberg, Berlin, Heidelberg
- Hornbogen E, Warlimont H, Skrotzki B (2019) Metalle: Struktur und Eigenschaften der Metalle und Legierungen, 7. Aufl. 2019. Springer Berlin Heidelberg, Berlin, Heidelberg
- Bhadeshia HKDH, Honeycombe RWK (2017) Steels: microstructure and properties, 4th edn. Elsevier Butterworth-Heinemann, Amsterdam, Boston, Heidelberg, London, New York, Oxford, Paris, San Diego, San Francisco, Singapore, Sydney, Tokyo
- Shubhank G, Aditi P, Ruchira N et al (2017) Processing and refinement of steel microstructure images for assisting in computerized heat treatment of plain carbon steel. *J Electron Imaging* 26:1. <https://doi.org/10.1117/1.JEI.26.6.063010>
- Eckstein H-J (1971) Waermebehandlung von Stahl: Metallkundliche Grundlagen: Mit 291 Bildern u. 24 Tab. Deutscher Verlag für Grundstoffindustrie VEB, Deutschland
- Ishida K (1995) Calculation of the effect of alloying elements on the Ms temperature in steels. *J Alloys Compounds* 220:126–131. [https://doi.org/10.1016/0925-8388\(94\)06002-9](https://doi.org/10.1016/0925-8388(94)06002-9)
- Su F, Wang H, Wen Z (2021) Modeling and simulation of dissolution process of bulk carbide in Fe–1C–1.44Cr low-alloy steel. *J Mater Res Technol* 11:992–999. <https://doi.org/10.1016/j.jmrt.2021.01.074>
- Capdevila C, Caballero FG, García De Andrés C (2003) Analysis of effect of alloying elements on martensite start temperature of steels. *Mater Sci Technol* 19:581–586. <https://doi.org/10.1179/026708303225001902>
- Lee S-J, Park K-S (2013) Prediction of martensite start temperature in alloy steels with different grain sizes. *Metall and Mat Trans A* 44:3423–3427. <https://doi.org/10.1007/s11661-013-1798-4>
- Schindelin J, Rueden C, Miura K et al (2016) Correctbleach: upgrade with exponential fitting method. Zenodo. <https://doi.org/10.5281/zenodo.58701>
- Benito S, Wulbieter N, Pöhl F et al (2019) Microstructural analysis of powder metallurgy tool steels in the context of abrasive wear behavior: a new computerized approach to stereology. *J of Materi Eng and Perform* 28:2919–2936. <https://doi.org/10.1007/s11665-019-04036-9>
- ASTM Standard practice for X-ray determination of retained austenite in steel with near random crystallographic orientation (E975-13), RIS, (2013)
- Su YY, Chiu LH, Chuang TL et al (2012) Retained austenite amount determination comparison in JIS SKD11 steel using quantitative metallography and X-ray diffraction methods. *Adv Compos Mater* 482-484:1165–1168. <https://doi.org/10.4028/www.scientific.net/AMR.482-484.1165>
- Tritt TM, Weston D (2004) Measurement techniques and considerations for determining thermal conductivity of bulk materials. In: Tritt TM (ed) *Thermal Conductivity*. Springer, US, pp 187–203
- Said Schicchi D, Caggiano A, Benito S et al (2017) Mesoscale fracture of a bearing steel: a discrete crack approach on static and quenching problems. *Theor Appl Fract Mech* 90:154–164. <https://doi.org/10.1016/j.tafmec.2017.04.006>
- Wu C, Xu W, Wan S et al (2022) Determination of heat transfer coefficient by inverse analyzing for selective laser melting (SLM) of AlSi10Mg. *Crystals* 12:1309. <https://doi.org/10.3390/cryst12091309>
- Xiong X-T, Liu X-H, Yan Y-M et al (2010) A numerical method for identifying heat transfer coefficient. *Appl Math Mod* 34:1930–1938. <https://doi.org/10.1016/j.apm.2009.10.010>
- John D'Errico (2006) fminsearchbnd: fminsearchcon. <https://de.mathworks.com/matlabcentral/fileexchange/8277-fminsearchbnd-fminsearchcon>. Accessed 22 Mar 2023
- Onsager L (1931) Reciprocal relations in irreversible processes. II. *Phys Rev* 38:2265–2279. <https://doi.org/10.1103/physrev.38.2265>
- Svoboda J, Fischer FD, Fratzl P et al (2004) Modelling of kinetics in multi-component multi-phase systems with spherical precipitates. *Mater Sci Eng A* 385:166–174. <https://doi.org/10.1016/j.msea.2004.06.018>
- Sonderegger B, Kozeschnik E (2009) Generalized nearest-neighbor broken-bond analysis of randomly oriented coherent interfaces in multicomponent Fcc and Bcc structures. *Metall and Mat Trans A* 40:499–510. <https://doi.org/10.1007/s11661-008-9752-6>
- Kozeschnik E, Svoboda J, Fischer FD (2006) Shape factors in modeling of precipitation. *Mater Sci Eng: A* 441:68–72. <https://doi.org/10.1016/j.msea.2006.08.088>
- Herrnring J, Sundman B, Staron P et al (2021) Modeling precipitation kinetics for multi-phase and multi-component systems using particle size distributions via a moving grid technique. *Acta Materialia* 215:117053. <https://doi.org/10.1016/j.actamat.2021.117053>
- Schaffnit P, Stallybrass C, Konrad J et al (2015) A Scheil–Gulliver model dedicated to the solidification of steel. *Calphad* 48:184–188. <https://doi.org/10.1016/j.calphad.2015.01.002>
- Staublerstahl (2023) 1.2379 Werkstoff Datenblatt. <https://www.staublerstahl.com/werkstoffe/12379-werkstoff-datenblatt/>. Accessed 25 May 2023
- Barbier D (2014) Extension of the martensite transformation temperature relation to larger alloying elements and contents. *Adv Eng Mater* 16:122–127. <https://doi.org/10.1002/adem.201300116>
- Schuppener J, Müller S, Benito S et al (2022) Short-term heat treatment of the high-alloy cold-work tool steel X153CrMoV12: calculation of metastable microstructural states. *steel research int*:2200452. <https://doi.org/10.1002/srin.202200452>
- Wiegand A (2016) Einsatz von Thermoelmenten: WIKA Datenblatt IN 00.23. https://www.wika.es/upload/DS_IN0023_de_de_51541.pdf. Accessed 28.08.2023
- Thermocouples - Part 3: Extension and compensating cables - Tolerances and identification system (IEC 60584-3:2021); German version EN IEC 60584-3:2021. <https://www.beuth.de/de/norm/din-en-iec-60584-3/346342654>. Accessed 28.08.2023
- Krauss G, Marder AR (1971) The morphology of martensite in iron alloys. *Metallurg Trans* 2:2343–2357. <https://doi.org/10.1007/BF02814873>
- Brodusch N, Demers H, Gauvin R (2013) Nanometres-resolution Kikuchi patterns from materials science specimens with transmission electron forward scatter diffraction in the scanning electron microscope. *J Microsc* 250:1–14. <https://doi.org/10.1111/jmi.12007>
- Gottstein G (2014) *Materialwissenschaft und Werkstofftechnik*. Springer Berlin Heidelberg, Berlin, Heidelberg
- Platl J, Leitner H, Turk C et al (2020) Determination of martensite start temperature of high-speed steels based on thermodynamic calculations. *Steel Research Int* 91:2000063. <https://doi.org/10.1002/srin.202000063>
- Peet M (2015) Prediction of martensite start temperature. *Mater Sci Technol* 31:1370–1375. <https://doi.org/10.1179/1743284714Y.0000000714>
- Qiao X, Han L, Zhang W et al (2016) Thermal stability of retained austenite in high-carbon steels during cryogenic and tempering treatments. *ISIJ Int* 56:140–147. <https://doi.org/10.2355/isijinternational.ISIJINT-2015-248>

36. Berns H (ed) (1998) Hartlegierungen und Hartverbundwerkstoffe: Gefüge, Eigenschaften, Bearbeitung Anwendung. Springer eBook Collection, Springer Berlin Heidelberg, Berlin, Heidelberg, s.1
37. Damon J, Dietrich S, Schulze V (2020) Implications of carbon, nitrogen and porosity on the $\gamma \rightarrow \alpha'$ martensite phase transformation and resulting hardness in PM-steel Astaloy 85Mo. *J Mater Res Technol* 9:8245–8257. <https://doi.org/10.1016/j.jmrt.2020.05.035>
38. Ko TH (2006) Numerical investigation on laminar forced convection and entropy generation in a curved rectangular duct with longitudinal ribs mounted on heated wall. *Int J Thermal Sci* 45:390–404. <https://doi.org/10.1016/j.ijthermalsci.2005.06.005>
39. Mola J, Ren M (2018) On the hardness of high carbon ferrous martensite. *IOP Conf Ser Mater Sci Eng* 373:12004. <https://doi.org/10.1088/1757-899X/373/1/012004>
40. Bhadeshia HKDH (1981) Thermodynamic extrapolation and martensite-start temperature of substitutionally alloyed steels. *Metal Sci* 15:178–180. <https://doi.org/10.1179/030634581790426697>
41. Hanumantharaju GAK (2018) Thermodynamic modelling of martensite start temperature in commercial steels, Sweden. <http://urn.kb.se/resolve?urn=urn:nbn:se:kth:diva-221719>. Accessed 28.08.2023.
42. Kroupa A (2013) Modelling of phase diagrams and thermodynamic properties using Calphad method—development of thermodynamic databases. *Comput Mater Sci* 66:3–13. <https://doi.org/10.1016/j.commatsci.2012.02.003>
43. Kozeschnik E, Buchmayr B (2001) MatCalc— A simulation tool for multicomponent thermodynamics, diffusion and phase transformation kinetics. *Mathematical Mod Weld Phenom*: 349–361. <https://graz.elsevierpure.com/en/publications/matcalc-a-simulation-tool-for-multicomponent-thermodynamics-diffu>
44. Nayak UP, Guitar MA, Mücklich F (2020) A comparative study on the influence of chromium on the phase fraction and elemental distribution in As-cast high chromium cast irons: simulation vs experimentation. *Metals* 10:30. <https://doi.org/10.3390/met10010030>
45. Schmidtseifer N, Weber S (2021) Microstructural changes during short-term heat treatment of martensitic stainless steel—simulation and experimental verification. *Metall Mater Trans A* 52:2885–2895. <https://doi.org/10.1007/s11661-021-06280-y>
46. Moumni Z, Roger F, Trinh NT (2011) Theoretical and numerical modeling of the thermomechanical and metallurgical behavior of steel. *Int J Plasticity* 27:414–439. <https://doi.org/10.1016/j.ijplas.2010.07.002>
47. Simsir C, Hunkel M, Lütjens J et al (2012) Process-chain simulation for prediction of the distortion of case-hardened gear blanks. *Mat.-wiss u Werkstofftech* 43:163–170. <https://doi.org/10.1002/mawe.201100905>
48. Eser A, Broeckmann C, Simsir C (2016) Multiscale modeling of tempering of AISI H13 hot-work tool steel—Part 1: Prediction of microstructure evolution and coupling with mechanical properties. *Comput Mater Sci* 113:280–291. <https://doi.org/10.1016/j.commatsci.2015.11.020>
49. Eser A, Broeckmann C, Simsir C (2016) Multiscale modeling of tempering of AISI H13 hot-work tool steel—Part 2: Coupling predicted mechanical properties with FEM simulations. *Comput Mater Sci* 113:292–300. <https://doi.org/10.1016/j.commatsci.2015.11.024>

Publisher's Note Springer Nature remains neutral with regard to jurisdictional claims in published maps and institutional affiliations.